JACS
JOURNAL OF THE AMERICAN CHEMICAL SOCIETY
pubs.acs.org/JACS
Article

Terminal, Open-Shell Mo Carbide and Carbyne Complexes: Spin Delocalization and Ligand Noninnocence

Gwendolyn A. Bailey, Joshua A. Buss, Paul H. Oyala, and Theodor Agapie*

Cite This: J. Am. Chem. Soc. 2021, 143, 13091−13102
Read Online
ACCESS | Metrics & More | Article Recommendations | Supporting Information

ABSTRACT: Open-shell compounds bearing metal−carbon triple bonds, such as carbides and carbynes, are of significant interest as plausible intermediates in the reductive catenation of C_1 oxygenates. Despite the abundance of closed-shell carbynes reported, open-shell variants are very limited, and an open-shell carbide has yet to be reported. Herein, we report the synthesis of the first terminal, open-shell carbide complexes, [**K**][**1**] and [**1**][$\mathbf{BAr^F_4}$] (**1** = P2Mo(≡C:)(CO), P2 = a terphenyl diphosphine ligand), which differ by two redox states, as well as a series of related open-shell carbyne complexes. The complexes are characterized by single-crystal X-ray diffraction and NMR, EPR, and IR spectroscopies, while the electronic structures are probed by EPR studies and DFT calculations to assess spin delocalization. In the d_1 complexes, the spin is primarily localized on the metal (∼55−77% Mo d_{xy}) with delocalization on the triply bonded carbon of ∼0.05−0.09 e^-. In the reduced carbide [**K**][**1**], a direct metal−arene interaction enables ancillary ligand reduction, resulting in reduced radical character on the terminal carbide (⩽0.02 e^-). Reactivity studies with [**K**][**1**] reveal the formation of mixed-valent C−C coupled products at −40 °C, illustrating how productive reactivity manifolds can be engendered through the manipulation of redox states. Combined, the results inform on the electronic structure and reactivity of a new and underrepresented class of compounds with potential significance to a wide array of reactions involving open-shell species.

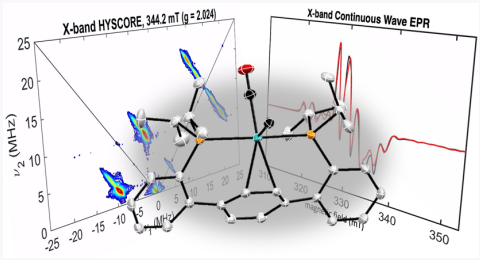

INTRODUCTION

Transition metal complexes that contain metal-to-ligand multiple bonds have been implicated in many important biological[1,2] and abiological reactions.[3,4] Of these, open-shell complexes are of special interest, and correlating reactivity with electronic structure, including spin delocalization, is an area of active pursuit.[5−20]

In such open-shell complexes, radical delocalization onto the multiply bonded ligand can vary widely, with important consequences for reactivity. In a study of the Mn nitrides $[Mn^{VI}(\equiv N:)(\text{salen-R})]^+$ (R = ^{t}Bu, CF_3, NMe_2), for example, the extent of spin delocalization onto the terminal nitride was strongly influenced by ancillary ligand electronics.[17] When R = NMe_2, a predominantly salen-centered radical was formed that resisted N−N coupling relative to the less electron-rich analogues studied.

Radical delocalization is also impacted by ligand geometry and metal d-electron count.[15,16,21] In electron-deficient d^1 and d^3 complexes, the unpaired electron often resides in low-lying $d_{x^2-y^2}$ and d_{xy} orbitals that are nonbonding with respect to the multiply bonded ligand. Spin delocalization onto the multiply bonded ligand may still arise but is typically minor. For example, in the trigonal-pyramidal d^3 complex $[Fe^V(\equiv N:)(L_3)][BAr^F_4]$ (L_3 = chelating tris(carbene) ligand), the unpaired spin was shown to populate a metal-based orbital of $3d_{xy}$ parentage orthogonal to the Fe−N bond vector, with only 0.12 e^- of unpaired spin populating the p_y and p_z orbitals on the nitride.[21,22] Similarly, the unpaired spin in the square-pyramidal d^1 phosphide $[P2Mo(\equiv P:)(Cl)][BAr^F_4]$ was localized predominantly in Mo $4d_{xy}$, with 0.10−0.14 e^- of spin density on the terminal phosphide.[18] Even small spin populations can have important consequences for reactivity, however. $[P2Mo^V(\equiv P:)(Cl)][BAr^F_4]$ underwent rapid bimolecular P−P coupling at −10 °C, unlike its closed-shell Mo^{IV} congener, which is stable at room temperature.[18] Likewise, $[Fe^V(\equiv N:)(\text{carbene})_3][BAr^F_4]$ reacts with water in the presence of cobaltocene to yield NH_3[23] in a mechanism that may involve PCET to an Fe(IV) imide. In these cases, there are differences in spin state as well as oxidation state, which complicates interpretation. Nevertheless, it is clear that the open-shell variants are particularly reactive and that further studies can help elucidate the structural and electronic aspects that drive reactivity.

In higher d-count complexes, the unpaired spin may populate metal-to-ligand antibonding orbitals, resulting in significantly greater spin delocalization to the ligand. In square-

Received: April 11, 2021
Published: August 11, 2021

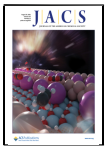

https://doi.org/10.1021/jacs.1c03806
J. Am. Chem. Soc. 2021, 143, 13091−13102

pyramidal Fe^{V} nitrides, for example, the SOMO of Fe−N π^* character is highly polarized toward the nitride, with up to 75% spin density located on the nitride and only 15−30% on Fe.[16,24,25] These complexes thus take on considerable Fe^{IV} character and can be considered nitridyl radicals. Likewise, ca. 50% spin density was found on the terminal nitride in trigonal Co^{IV} and square-planar Ir^{IV} complexes, with the balance localized on the metal.[26,27] Significant spin delocalization is also found in many electron-rich, open-shell *carbene* complexes.[28−30] While stabilized by interaction with the metal center, these ligands behave like organic radicals and thus have found application in a range of catalytic reactions.[14,30−40]

Relative to open-shell oxo and nitride complexes,[41,42] open-shell carbyne complexes are extremely rare. The small number reported of any kind[43−51] stands in contrast to the plethora of closed-shell examples.[52,53] Of those terminal examples characterized structurally,[43−50] only three have been characterized by methods that address the spin localization.[47,48,54] Relative to carbynes, *carbide* complexes ([M]≡C:) are rarer still.[55] Terminal, closed-shell examples are limited to the d^6 group 8 examples of the type $[M(\equiv C:)(L)_2(X)_2]$ (M = Ru, Os),[56−59] the d^2/d^0 group 6 examples $[Tp^*(CO)_2M(\equiv CLi)]$ (M = W, Mo) and $[\{N(R)Ar\}_3Mo(\equiv C:)]^-$ (Tp^* = 3,5-dimethyl tris(pyrazolyl)borate),[60−63] and most recently, the d^2 group 6 examples P2Mo(≡C:)(CO) **1** and its coordination isomer PMo(≡C:)(CO)P (P2 = terphenyl diphosphine ligand; see Scheme 1 and Figure 11 for structures).[64−66] To our knowledge, a well-characterized example of an open-shell, terminal carbide complex has yet to be reported.

Scheme 1. Synthesis of Open-Shell Carbide Complexes[a]

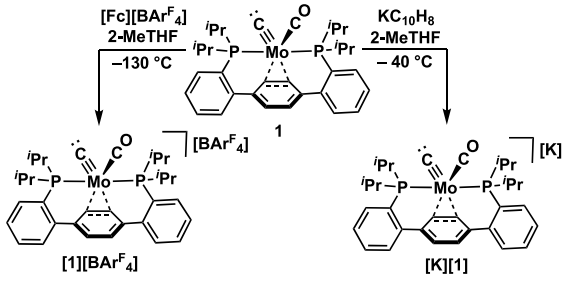

[a]$KC_{10}H_8$ = potassium naphthalenide; $[BAr^F_4]^-$ = tetrakis[3,5-bis(trifluoromethyl)phenyl] borate; $[Fc]^+$ = ferrocenium; 2-MeTHF = 2-methyltetrahydrofuran.

Nonetheless, reactive transition metal carbides and carbynes are of considerable interest in the context of hydrogenation and C−C coupling of C_1 oxygenates.[55,67−72] Toward harnessing the full potential of reactive, open-shell carbides and carbynes in catalysis, there is need to first develop robust synthetic strategies toward these compounds and to understand how spin delocalization can be controlled through metal d-electron count and ligand choice. Herein, we report the synthesis and detailed characterization of the first terminal, open-shell carbides [**1**][**BAr$^F_4$**] and [**K**][**1**] as well as a series of structurally related carbynes, [**2**][**BAr$^F_4$**]−[**4**][**BAr$^F_4$**] (**1** = P2Mo(≡C:)(CO); **2**, **3** = P2Mo(≡CR)(CO)(Cl), R = H, $SiMe_3$; **4** = P2Mo(≡$CSiMe_3$)(Cl)). The synthesis of [**1**][**BAr$^F_4$**] and [**K**][**1**] is enabled by the versatility of the P2 ligand, which is capable of flexible coordination modes and storage of reducing equivalents. Detailed electron paramagnetic resonance (EPR) studies are coupled with density functional theory (DFT) calculations to quantitatively assess the spin delocalization. Preliminary reactivity studies are presented in which reduced carbides are coupled intramolecularly to form mixed-valent, C−C bridged dimers.

RESULTS AND DISCUSSION

Synthesis and Characterization of Open-Shell Carbide Complexes. Open-shell carbide complexes [**1**][**BAr$^F_4$**] and [**K**][**1**] were targeted from d^2 carbide **1**, which was prepared *in situ* via deprotonation and Cl loss from methylidyne P2Mo(≡CH)(CO)(Cl) **2** according to the literature methods.[66] Thus, [**1**][**BAr$^F_4$**] was successfully prepared by treatment of thawing solutions of **1** with [Fc][BAr^F_4] at −130 °C in 2-MeTHF (Scheme 1). The X-band CW-EPR spectrum of a frozen glass of this deep brown solution at 77 K revealed a complex, primarily axial signal with g_{iso} = 2.009, consistent with generation of the expected S = 1/2 cation (Figure 1a). Warming the solution beyond −130 °C resulted in loss of the EPR signal, illustrating the extreme thermal sensitivity of this species.

The CW-EPR spectra of this complex were well-simulated using a slightly rhombic **g**-tensor with g = [2.0247, 2.0190, 1.9837] (Table 1). Hyperfine couplings to $^{95/97}$Mo ($|A(^{95/97}Mo)|$ = [86, 86, 154] MHz) and two ^{31}P nuclei ($|A(^{31}P)|$ = [75, 80, 52] and [45, 58, 50] MHz) were observed, indicating that both arms of the P2 ligand remain bound upon oxidation (Table 2). The hyperfine couplings and **g**-tensor are similar to those of previously characterized open-shell phosphide complex [P2Mo(≡P:)(Cl)][BAr^F_4],[18] indicating electronic and structural similarity. The final $^{95/97}$Mo and ^{31}P hyperfine coupling parameters above were also constrained through simulations of X-band Davies electron nuclear double resonance (ENDOR) measurements conducted at 25 K (Figure 2). Though both magnetic isotopes of Mo are high spin—^{95}Mo (I = 5/2, 15.92%) and ^{97}Mo (I = 5/2, 9.55% abundant)—and thus could be expected to exhibit additional fine structure from the nuclear quadrupole interaction, we did not observe any clearly resolved quadrupole splittings in the Mo-associated ENDOR signals for any of the complexes in this study. This indicates that the quadrupole splittings are small in comparison to the ENDOR line width and $^{95/97}$Mo hyperfine anisotropy.

Additional hyperfine couplings to the ^{13}C(carbide) and ^{13}C(CO) nuclei were detected in the isotopically enriched derivative [**1**-^{13}**C$_2$**][**BAr$^F_4$**], which is prepared via oxidation of previously reported[66] **1**-^{13}**C$_2$** and bears labels at the carbide and CO carbons (see the Supporting Information). Hyperfine sublevel correlation (HYSCORE) spectra of [**1**-^{13}**C$_2$**][**BAr$^F_4$**] showed signals consistent with couplings to two distinct ^{13}C nuclei which exhibited similar isotropic couplings but varying degrees of anisotropy ($|A(^{13}C_A)|$ = [15, 11, 9] MHz; $|A(^{13}C_B)|$ = [8, 22, 8] MHz; Figure 3). To confirm the signal observed is not due to oxidation of residual **2** from in situ preparation of **1**, methylidyne [**2**][**BAr$^F_4$**] was independently prepared and found to exhibit a different CW-EPR signature from [**1**][**BAr$^F_4$**] (Figure S2).

Reduced carbide [**K**][**1**] was synthesized via addition of a freshly prepared, thawing solution of potassium naphthalenide (1 equiv) to a thawing solution of **1** (Scheme 1). A dramatic color change from red-brown to deep teal was evident on mixing, and the 77 K X-band CW-EPR spectrum of a frozen glass of this solution indeed revealed formation of a new S = 1/

https://doi.org/10.1021/jacs.1c03806
J. Am. Chem. Soc. 2021, 143, 13091−13102

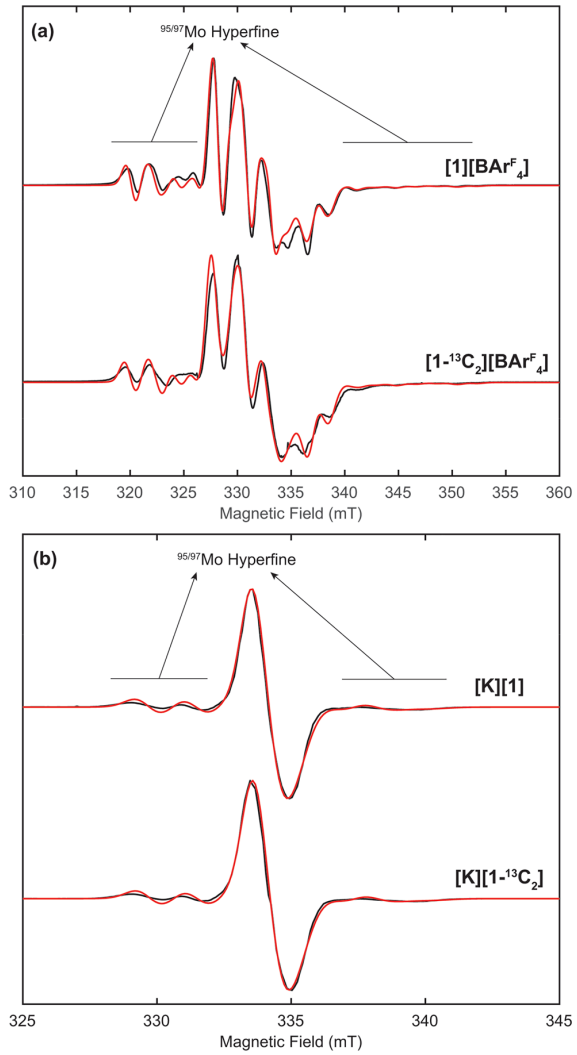

Figure 1. X-band CW-EPR spectra (black) of (a) [**1**][**BAr$^F_4$**] and (b) [**K**][**1**] with natural abundance (top) and ^{13}C enrichment (bottom) at a temperature of 77 K with spectral simulations overlaid (red; parameters in Tables 1 and 2). Acquisition parameters: MW frequency = 9.324−9.385 GHz; MW power = 200 μW ([**1**][**BAr$^F_4$**]) or 20 μW ([**K**][**1**]); modulation amplitude = 0.2 mT; conversion time = 82 ms.

Table 1. Experimentally Determined *g*-Values for Open-Shell Carbides [1][BAr$^F_4$] and [K][1]

complex	g_x	g_y	g_z	g_{iso}
[**1**][**BAr$^F_4$**]	2.0247	2.0190	1.9837	2.0091
[**K**][**1**]	2.0060	2.0015	1.9980	2.0018

2 cation with visible hyperfine couplings to Mo (Figure 1b). [**K**][**1**] proved significantly more stable than [**1**][**BAr$^F_4$**], persisting in solution up to at least −40 °C. Single crystals were obtained by encapsulation of K^+ with 18-crown-6 (1 equiv) followed by diffusion of pentane into concentrated solutions in 2-MeTHF at −40 °C.

Analysis of the XRD structure confirmed generation of [**K(18-crown-6)**][**1**] (Figure 4). The structure of [**1**]$^-$ exhibits pseudo-square-pyramidal ligand geometry (τ_5 = 0.19) similar to that observed for the previously reported nitride and phosphide derivatives [P2Mo(≡E:)(Cl)]$^{n+}$ (E = N, P; n = 0, 1).[18,73] The carbide ligand is located at the axial position, and the CO ligand is trans to an η^2(C, C)-interaction with the central arene ring. The Mo≡C: distance is 1.739(5) Å, slightly shorter than previously reported Mo^{IV} *carbyne* complexes of the same ligand platform (1.764(2)−2.032(1) Å)[64−66] but similar to that reported for the Mo^{VI} carbide [Mo(≡C:)(N(R)Ar)$_3$]$^-$ (1.713(9) Å).[60]

Compared to [**1**][**BAr$^F_4$**], the 77 K X-band CW-EPR spectrum of [**K**][**1**] exhibits significantly reduced anisotropy in the **g**-tensor with g = [2.006, 2.0015, 1.998] and g_{iso} ∼ 2, suggesting more delocalized radical character (Figure 1b and Table 1). The g values for [**K**][**1**] may be compared to those of the predominantly metal-centered Mo(III) complexes, [Mo(L)(trisamidoamine)] in which L = CO and N_2, where the unpaired spin is degenerately located in π-backbonding orbitals of d_{xy}, d_{xz} origin and g is significantly more anisotropic with $g_{\parallel}$, $g_{\perp}$ = 3.03, 1.51.[74] Comparatively small hyperfine couplings to $^{95/97}$Mo ($|A(^{95/97}\text{Mo})|$ = [46, 46, 59] MHz) and two ^{31}P nuclei ($|A(^{31}\text{P})|$ = [8.4, 3.6, 3.6]) were observed in the CW-EPR and Davies ENDOR spectra (Table 2 and Figure S14). Relatively weak hyperfine couplings to two inequivalent ^{13}C nuclei ($|A(^{13}\text{C})|$ = [4.6, 5.5, 5.5] and [−0.05, −0.05, 4.5] MHz) were measured via HYSCORE spectroscopy of the labeled derivative, [**K**][**1**-$^{13}C_2$] (Figures S15−S20). The small magnitudes of these couplings preclude a carbide-centered radical and suggest that the unpaired spin may instead be primarily located on the arene system of the P2 ligand.[64,65]

Radical Delocalization in [1][BAr$^F_4$] and [K][1] as Revealed by Spin Decomposition Analysis of the Hyperfine Coupling Tensors and DFT Calculations. To more quantitatively assess spin delocalization in [**1**][**BAr$^F_4$**] and [**K**][**1**], the hyperfine coupling tensors were decomposed into their s- and p-orbital origins using the method of Hoffman and co-workers.[21,75] Thus, compared to an electron in a 5s orbital of ^{95}Mo for which $|a^0_{iso}(^{95}\text{Mo})|$ = 1984 MHz,[76] a_{iso} = 107 MHz for [**1**][**BAr$^F_4$**] corresponds to a small Mo 5s spin density of ∼0.05 e$^-$. Taking a unit of unpaired spin in the Mo $4d_{xy}$ orbital with the z-axis extending along the Mo−carbide bond, the anisotropic component T = [−23, −23, 47] MHz corresponds to a spin density in Mo $4d_{xy}$ of ∼0.53 e$^-$ ($|\rho_{tot}|$ = 0.58 e$^-$, Table 2; Mo $T^0_{d_{xy}}$ = [−43.1, −43.1, 86.2] MHz and $A(^{95/97}\text{Mo}) = a_{iso} + T$; see the Supporting Information for details).[76]

The ^{13}C hyperfine coupling for the carbide nucleus was treated similarly. However, the measured hyperfine couplings to the two ^{13}C nuclei (denoted $^{13}C_A$ and $^{13}C_B$ to indicate ambiguous assignment) could not be definitively assigned to the respective carbide and ^{13}CO nuclei, and thus were each considered separately.[77] Each nucleus exhibits an isotropic coupling of a_{iso} ∼ 12 that when compared to the expected coupling of an electron in a 2s orbital $|a^0_{iso}(^{13}\text{C})|$ = 3777 MHz[76] yielded a small 2s orbital density of ∼0.003 e$^-$.

The 2p orbital density was treated similarly, following subtraction of the nonlocal contribution T^{∞}_{nloc} = [−2.2, −2.2, 4.5] MHz due to the through-space dipolar interaction between the ^{13}C nucleus and the unpaired spin density at the Mo nucleus.[21,75] Following subtraction of T^{∞}_{nloc}, $^{13}C_A$ and $^{13}C_B$ each yielded a similar predicted carbide spin density of 0.06−0.09 e$^-$ in the C 2p orbitals, orthogonal to the Mo≡C:

https://doi.org/10.1021/jacs.1c03806
J. Am. Chem. Soc. 2021, 143, 13091−13102

Table 2. Hyperfine Coupling Tensors (in MHz) Measured for [1][BAr$^F_4$] and [K][1], with Total Spin Populations $|\rho_{tot}|$ Estimated According to the Experimentally Measured Hyperfine Coupling Tensors[a]

complex		A_x	A_y	A_z	a_{iso}	$\lvert\rho_{tot}\rvert$
[1][BAr$^F_4$]	$^{95/97}$Mo[b]	86	86	154	109	0.58
	$^{31}P_A$	75	80	52	69	
	$^{31}P_B$	45	58	50	51	
	$^{13}C_A$	15	11	9	11.7	0.06−0.09[c]
	$^{13}C_B$	8	22	8	12.7	0.05−0.07[d]
[K][1]	$^{95/97}$Mo[b]	46	46	59	50.3	0.12−0.20
	P_A	8.4	3.6	3.6	5.2	
	P_B	8.4	3.6	3.6	5.2	
	$^{13}C_A$	−0.05	−0.05	4.5	1.5	⩽0.02[c]
	$^{13}C_B$	4.6	5.5	5.5	5.2	

[a]Signals observed for the ^{31}P and ^{13}C nuclei cannot be definitively assigned and thus are denoted A and B. [b]Hyperfine values are only reported for the more abundant ^{95}Mo (I = 5/2, 15.92%), but simulations also include contributions from ^{97}Mo (I = 5/2, 9.55%). [c]Estimated spin density for the carbide C31. [d]Estimated spin density for the CO ligand C32.

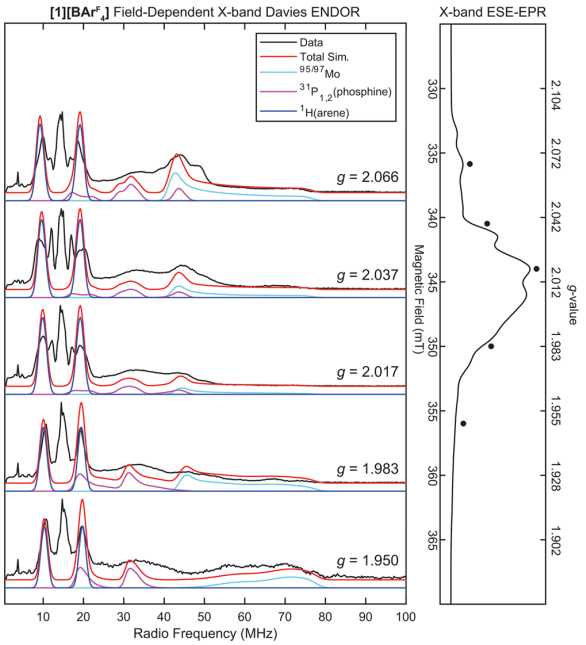

Figure 2. Field-dependent X-band Davies ENDOR spectra of natural abundance [1][BAr$^F_4$] (black) with simulations overlaid (parameters in Table 2). The electron spin echo (ESE) detected EPR spectrum is shown to the right, with fields at which ENDOR was acquired denoted with black circles. Acquisition parameters: temperature = 25 K; MW frequency = 9.716 GHz; MW π pulse length = 80 ns; interpulse delay τ = 240 ns; π_{RF} pulse length = 15 μs; T_{RF} delay = 2 μs; shot repetition time (srt) = 5 ms.

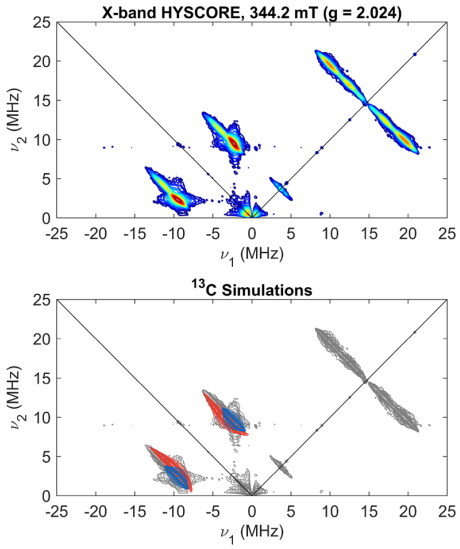

Figure 3. Top: X-band HYSCORE spectrum of [1-$^{13}C_2$][BAr$^F_4$] (top) measured at 344.2 mT (g = 2.024). Bottom: overlay of ^{13}C simulation contours ($^{13}C_A$ in blue, $^{13}C_B$ in red) with experimental contours (gray). Experimental conditions: temperature = 25 K; MW frequency = 9.716 GHz; τ = 136 ns; $t_1 = t_2$ = 100 ns; $\Delta t_1 = \Delta t_2$ = 16 ns; shot repetition time (srt) = 3 ms. For additional spectra measured at other magnetic fields and comparison with data of natural abundance [1][BAr$^F_4$], see Figures S8−S13.

bond vector. Similarly, following subtraction of T^x_{nloc} or T^y_{nloc} from $^{13}C_A$ and $^{13}C_B$ (in a direction perpendicular to the carbide in the molecular frame), the same analysis of $^{13}C_A$ and $^{13}C_B$ yielded a predicted spin density of 0.05−0.07 e$^-$ on ^{13}CO.

Decomposition of the hyperfine coupling tensors for [K][1] revealed significantly reduced spin density on both Mo (∼0.13−0.20 e$^-$) and carbide C31 (⩽0.02 e$^-$) relative to [1][BAr$^F_4$]. As with [1][BAr$^F_4$], the majority of the spin density was found to be located in carbide 2p orbitals, with only a small proportion in C 2s (⩽0.001 e$^-$). The remaining spin density (ca. 0.89 e$^-$ according to a Löwdin population analysis; see below) was instead found to reside on the terphenyl arene unit. Experimental evidence for occupation of this orbital by the unpaired electron is derived from examination of the crystallographic bond metrics. Relative to the closest structurally characterized Mo^{IV} analogue, P2Mo(≡CSiMe$_3$)(CO)(Cl) **3′** in which the silylcarbyne ligand is oriented cis to the η^2-arene interaction,[65] the terphenyl arene bond distances in [K][1] display the expected pattern of elongation and contraction based on population of the DFT-calculated SOMO, most notably in the central arene ring and flanking arene−arene linkages (Figure 5). The increased electron density in the central arene is also reflected in the direct contacts with the K$^+$ ion at the electron-rich C4−C5 positions (Figure 4). Notably, the formally anionic carbide ligand does not interact with K$^+$, although this could be due to

https://doi.org/10.1021/jacs.1c03806
J. Am. Chem. Soc. 2021, 143, 13091−13102

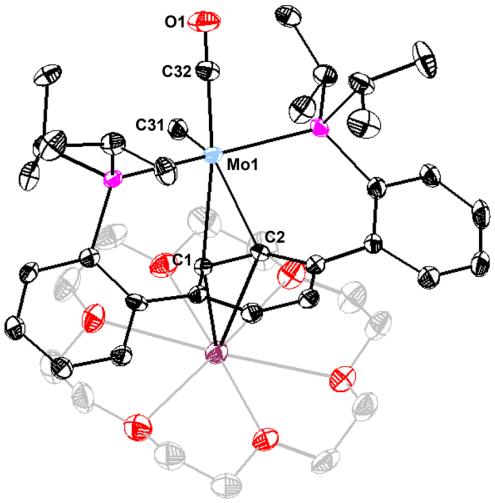

Figure 4. Solid-state structure of [**K**(**18-crown-6**)][**1**]. Thermal anisotropic displacement ellipsoids are shown at the 50% probability level. H atoms are omitted for clarity. Key bond lengths (Å) and angles (deg): Mo1−C31 1.739(5); Mo1−C32 1.974(6); C32−O1 1.157(8); Mo1−C1 2.444(5); Mo1−C2 2.449(5); C1−C2 1.390(7).

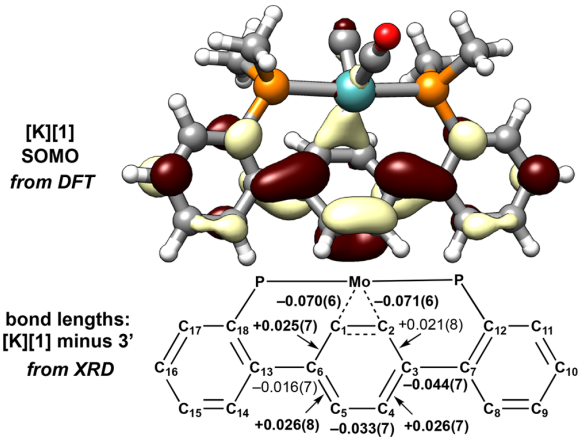

Figure 5. Crystallographically determined bond elongations and contractions on reduction of the arene unit by one electron. Top: DFT-calculated SOMO for [**K**][**1**] (BP86/def2-TZVP; isosurfaces at 0.04 e$^-$ Å). Bottom: bond length difference map for the terphenyl arene moiety of [**K**][**1**] minus that of Mo(IV) comparator P2Mo(≡CSiMe$_3$)(CO)(Cl) **3′** (the kinetic isomer of **3** in which the CO ligand is oriented trans to the Mo−arene interaction; see Chart S2 for structure)[64] showing elongated and contracted bonds for [**K**][**1**] according to the anticipated π-bonding or antibonding character (95% certainty or better; ≥99.7% certainty values are indicated in bold).

steric constraints between the isopropyl substituents and the encapsulating crown ether.[60,63]

Further insight into the nature of Mo≡C: bonding and spin delocalization in [**1**][**BAr$^F_4$**] and [**K**][**1**] was obtained via DFT calculations using unrestricted Kohn−Sham methods with the BP86 functional and def2-TZVP basis set. The structures of [**1**][**BAr$^F_4$**] and [**K**][**1**] converged to minimum-energy geometries as depicted in Scheme 1 with no imaginary frequencies (Figure S36). (Similar agreement was found for the crystallographically characterized carbyne complexes [**2**]-[**BAr$^F_4$**]−[**4**][**BAr$^F_4$**] below at the same level of theory.)

Single-point energy calculations were conducted on the optimized geometries for [**K**][**1**] and [**1**][**BAr$^F_4$**] and compared with previously reported **1** at the same level of theory.[65] Comparison of the orbital contours revealed a close correspondence in their electronic structures. The Mo−carbide bonding can be described as a formally triple bond with one high-lying σ-bonding MO and two lower-energy π-bonding MOs (Figure 6). As indicated by the EPR measurements

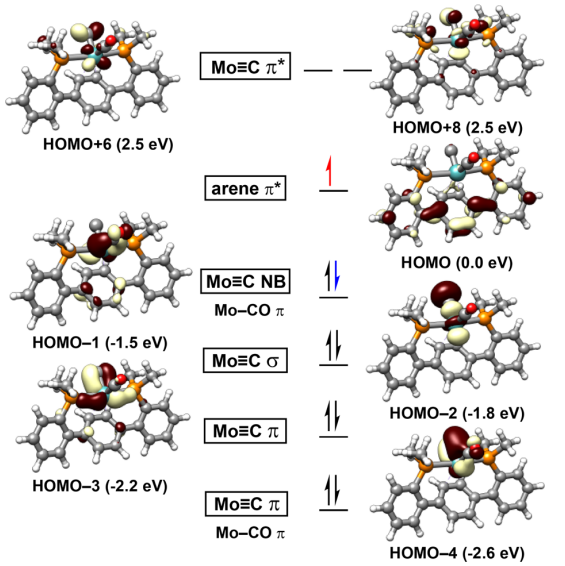

Figure 6. Qualitative MO diagram for [**1**][**BAr$^F_4$**] (black), **1** (blue), and [**K**][**1**] (red) depicting the Mo≡C: bonding interaction and SOMOs. Calculated α molecular orbitals (isosurfaces at 0.05 e$^-$ Å^{-3}) and orbital energy levels are depicted for [**1**]$^-$; β molecular orbitals for [**K**][**1**], and MO diagrams for [**1**][**BAr$^F_4$**]−[**4**][**BAr$^F_4$**] are provided in Figures S38−S47.

above, the HOMO in both [**1**][**BAr$^F_4$**] and **1** is of Mo 4d$_{xy}$ parentage and is strictly nonbonding with respect to the carbide; this orbital has backbonding character with respect to the Mo−CO interaction. The electronic structures are similar to the phosphide [P2Mo(≡P:)(Cl)]$^{n+}$ (n = 0, 1),[18] except the M≡E: σ orbital is lower energy relative to the π orbitals in the terminal phosphide complex, reflecting differences in σ vs π orbital overlap of the carbide ligand relative to the phosphide.

In accordance with the MO diagrams, the calculated Löwdin spin populations predict that the majority of spin density rests in the Mo 4d$_{xy}$ orbital (+0.55 e$^-$), with 0.07 e$^-$ of negative spin polarization on the carbide, as visualized through the spin density plots (Figure 7). Overall, the Löwdin spin densities at Mo, ^{13}C(carbide), and ^{13}C(CO) for this complex agree well with the experimental findings from EPR (see Table 5).

In [**K**][**1**], the HOMO−1 of 4d$_{xy}$ parentage shows a close correspondence with the SOMO of [**1**][**BAr$^F_4$**] and is occupied by two electrons. The next lowest energy orbital contains an unpaired electron and is of largely arene-based character (Figure 6). The combined EPR, DFT, and crystallographic data thus support a much more delocalized spin for [**K**][**1**] relative to [**1**][**BAr$^F_4$**], which nearly eliminates localization of spin density on the carbide ligand (+0.02 e$^-$

https://doi.org/10.1021/jacs.1c03806
J. Am. Chem. Soc. 2021, 143, 13091−13102

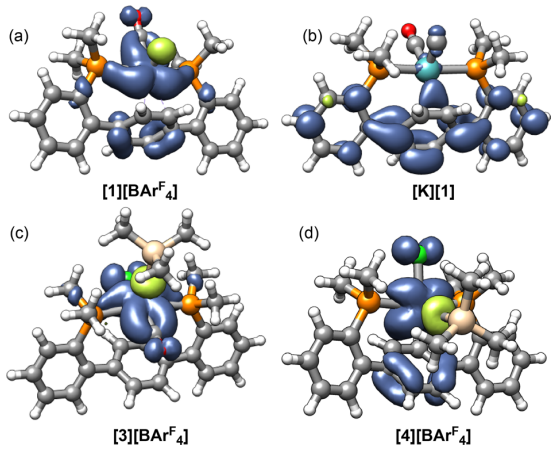

Figure 7. DFT-calculated spin density plots and Löwdin spin populations (BP86/def2-TZVP) for (a) [**1**][**BAr$^F_4$**], (b) [**K**][**1**], (c) [**3**][**BAr$^F_4$**], and (d) [**4**][**BAr$^F_4$**]. Atoms are shown scaled at 50%; H atoms are omitted for clarity (isosurfaces at 0.0016 e$^-$ Å^{-3}).

according to a Löwdin population analysis; Figure 7b and Table 5). Apparently, the direct metal−arene interaction in [**K**][**1**] enables ancillary ligand reduction prior to population of the Mo−carbide antibonding orbitals, leading to reduced spin density at the carbide and presumably enhancing the thermal robustness of [**K**][**1**].

Synthesis and Characterization of Open-Shell Carbyne Complexes, [2][BAr$^F_4$]−[4][BAr$^F_4$]. Relative to [**1**][**BAr$^F_4$**], the open-shell carbyne complexes [**2**][**BAr$^F_4$**]−[**4**][**BAr$^F_4$**] are comparatively robust. To gain solid-state structural information about Mo^V≡C complexes and to probe the impact of changes in the ligand sphere on spin delocalization in Mo(V) complexes, the methylidyne [**2**][**BAr$^F_4$**], silylcarbyne [**3**][**BAr$^F_4$**], and CO-free silylcarbyne [**4**][**BAr$^F_4$**] were prepared. The CO-bound derivatives [**2**][**BAr$^F_4$**] and [**3**][**BAr$^F_4$**] were prepared via one-electron oxidation of the corresponding Mo(IV) analogues (**2** and **3**)[64,66] with [Fc][BAr$^F_4$] in thawing 2-MeTHF (Scheme 2a). Isolation of [**2**][**BAr$^F_4$**] and [**3**][**BAr$^F_4$**] necessitated precipitation and washing at temperatures ⩽−40 °C to prevent CO loss (*vide infra*). Both complexes feature a high-energy CO stretch, consistent with diminished CO activation on oxidation. The CO stretching frequency in [**2**][**BAr$^F_4$**] is observed at 2070 cm^{-1} (cf. 1852 cm^{-1} in **2**) while that of [**3**][**BAr$^F_4$**] is observed at 2049 and 1971 cm^{-1}, possibly because of the presence of two isomers in the solid state (cf. 1852 cm^{-1} in **2** and 1873 cm^{-1} in **3**). Only one frequency is recorded at 1967 cm^{-1} in THF solutions, however, potentially indicating fluxional behavior.[64,66]

Scheme 2. Synthesis of Open-Shell Carbyne Complexes [2][BAr$^F_4$]−[4][BAr$^F_4$]

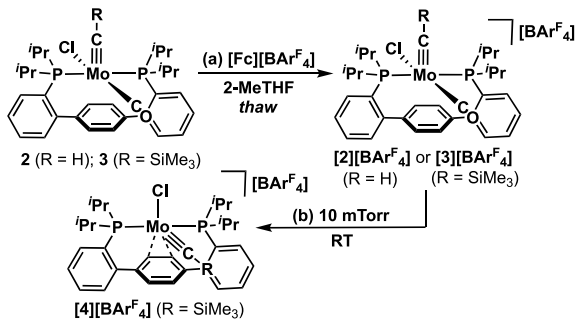

Both [**2**][**BAr$^F_4$**] and [**3**][**BAr$^F_4$**] proved amenable to solid-state characterization via single-crystal XRD. These studies confirmed that the ligand binding mode remains unchanged on oxidation (Figure 8; for the structure of [**3**][**BAr$^F_4$**], see Figure S50). In each complex, the Mo center is situated considerably above the arene ring (e.g., ca. 3.1 Å in [**2**][**BAr$^F_4$**]), precluding any direct Mo−arene contact. The remaining ligands adopt a pseudo-square-pyramidal geometry (τ_5 = 0.09) with the carbyne ligand occupying the axial position. The Mo≡C distance in [**2**][**BAr$^F_4$**] (1.753(2) Å) is within the expected range for a triple bond and is only slightly contracted relative to **2** (1.764(2) Å).[66] This bond contraction could reflect the reduced ionic radius of Mo[60] or increased electrostatic interactions between Mo(V) and C^{3-}. A similar contraction was observed on oxidation of a d^2 benzylidyne complex, W(CPh)(dmpe)$_2$Br, by [C_7H_7][PF_6] (0.024 Å).[45] The solid-state structure of [**2**][**BAr$^F_4$**] also revealed significant elongation in the Mo−CO bond (2.095(2) Å, vs 1.930(4) Å in **2**) and shortening of the Mo−Cl bond (2.3615(7) Å, vs 2.548(1) Å in **2**), consistent with the orbital picture developed in which the SOMO of d_{xy} parentage has π-backbonding character with respect to CO and π^*-antibonding character with respect to Cl (similarly to carbide [**1**][**BAr$^F_4$**] above and consistent with DFT calculations; see Figures S42 and S43).

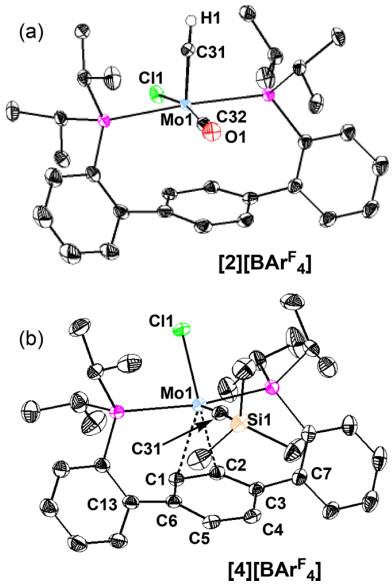

Figure 8. Solid-state structures of (a) [**2**][**BAr$^F_4$**] and (b) [**4**][**BAr$^F_4$**]. Thermal anisotropic displacement ellipsoids are shown at the 50% probability level. [BAr$^F_4$]$^-$ counterions and H atoms are omitted for clarity, except the methylidyne H atom in [**2**][**BAr$^F_4$**], which was located in the electron density map and refined freely. Key bond lengths (Å) and angles (deg): [**2**][**BAr$^F_4$**]: Mo1−C31 1.753(2); Mo1−C32 2.095(2); C32−O1 1.128(3); Mo−Cl 2.3615(7). [**4**][**BAr$^F_4$**]: Mo1−C31 1.734(9); Mo1−Cl1 2.355(2); Mo1−C1 2.423(6); Mo1−C2 2.445(6); C1−C2 1.363(9). For the structure of [**3**][**BAr$^F_4$**], see Figure S50.

https://doi.org/10.1021/jacs.1c03806
J. Am. Chem. Soc. 2021, 143, 13091−13102

Consistent with reduced backbonding to the CO ligand, both [**2**][$\mathbf{BAr^F_4}$] and [**3**][$\mathbf{BAr^F_4}$] proved susceptible to CO loss, even at RT in the solid state. Thus, a color change from green ([**2**][$\mathbf{BAr^F_4}$]) or pink ([**3**][$\mathbf{BAr^F_4}$]) to purple or maroon was observed over a period of weeks to months at RT, accompanied by a disappearance of the CO stretching frequencies in the IR spectra (Figure S35). Alternatively, CO loss was induced through extensive trituration and in vacuo drying of [**3**][$\mathbf{BAr^F_4}$] (Scheme 2b). According to the EPR and IR analyses, CO loss was incomplete in some samples (e.g., Figure 9b), likely reflecting trapping within larger microcrystals. Attempts to obtain clean samples were not reproducible, as competing decomposition was also observed in some cases.

Nonetheless, CO loss was confirmed in a single crystal XRD study of silylcarbyne [**4**][$\mathbf{BAr^F_4}$] (Figure 8b). The structure of [**4**][$\mathbf{BAr^F_4}$] is disordered with ca. 20% of the Mo(IV) complex [P2Mo(CO)($CSiMe_3$)][BAr^F_4], presumably reflecting disproportionation under the conditions of crystallization (Figure S51). A pseudo-square-pyramidal geometry is again assumed in [**4**][$\mathbf{BAr^F_4}$] with the silylcarbyne moiety in the apical position, but this time an η^2-C,C interaction was observed to the central terphenyl arene, similarly to in carbide [**K**][**1**]. Of note, however, the silylcarbyne ligand projects over the central arene ring, in contrast to [**K**][**1**] where it faces in the opposite direction.[78] The Mo≡CR distance (1.734(9) Å) is comparable to that of [**2**][$\mathbf{BAr^F_4}$] and [**K**][**1**] above, confirming retention of the triple bond.

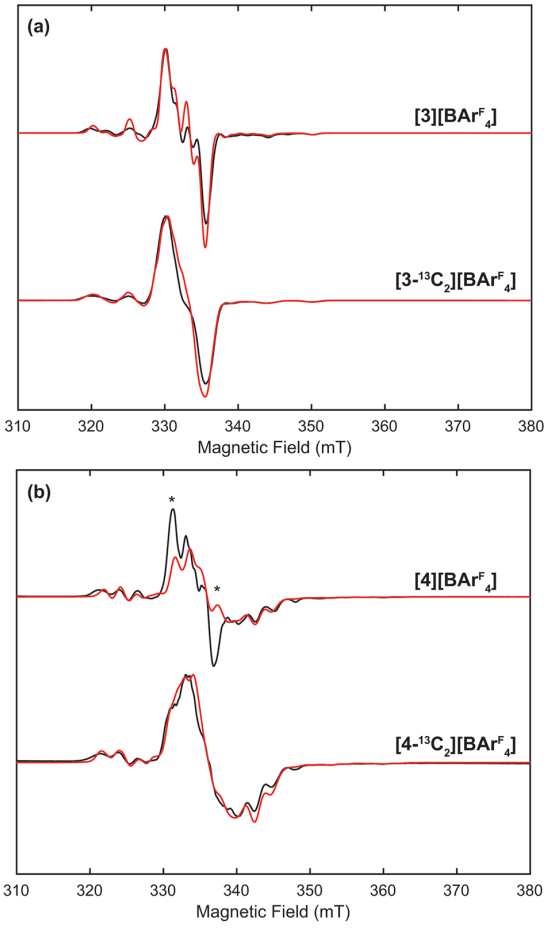

Figure 9. X-band CW-EPR spectra (black) of (a) [**3**][$\mathbf{BAr^F_4}$] and (b) [**4**][$\mathbf{BAr^F_4}$] with natural abundance (top) and ^{13}C enrichment (bottom) at a temperature of 77 K with spectral simulations overlaid (red; parameters in Tables 3 and 4). Acquisition parameters: MW frequency = 9.324−9.385 GHz; MW power = 200 μW; modulation amplitude = 0.2 mT; conversion time = 82 ms. Asterisks indicate features associated with residual [**3**][$\mathbf{BAr^F_4}$] due to incomplete CO loss. For the CW-EPR spectra of [**2**][$\mathbf{BAr^F_4}$] and its $^{13}C_2$ analogue, see Figure S2.

EPR and DFT Studies of [2][$\mathbf{BAr^F_4}$]−[4][$\mathbf{BAr^F_4}$]. To probe electronic structure and spin delocalization in the open-shell carbyne complexes, in-depth EPR and DFT studies were pursued. As for [**1**][$\mathbf{BAr^F_4}$], the 77 K X-band CW-EPR spectra of [**2**][$\mathbf{BAr^F_4}$]−[**4**][$\mathbf{BAr^F_4}$] were well-simulated with slightly rhombic **g**-tensors and couplings to two ^{31}P nuclei and a single $^{95/97}Mo$ nucleus consistent with generation of the expected cations (Figure 9 and Table 3). As well, couplings to two inequivalent ^{13}C nuclei were refined via ENDOR spectroscopy with labeled [**3**-$^{13}\mathbf{C_2}$][$\mathbf{BAr^F_4}$] and only one for [**4**-^{13}**C**][$\mathbf{BAr^F_4}$] via HYSCORE (Figures S21−S32). The CW-EPR spectra for [**2**][$\mathbf{BAr^F_4}$] (Figure S2) were satisfactorily simulated by using the parameters in Tables 3 and 4, though the simulations were not refined through pulse experiments.[79]

Table 3. Experimentally Determined *g*-Values for [2][$\mathbf{BAr^F_4}$], [3][$\mathbf{BAr^F_4}$], and [4][$\mathbf{BAr^F_4}$]

complex	g_x	g_y	g_z	g_{iso}
[**2**][$\mathbf{BAr^F_4}$]	2.0275	2.0175	1.9960	2.0137
[**3**][$\mathbf{BAr^F_4}$]	2.0286	2.0082	1.9970	2.0113
[**4**][$\mathbf{BAr^F_4}$]	2.0145	2.0030	1.9620	1.9932

Table 4. Hyperfine Coupling Tensors (in MHz) Measured for Oxidized Complexes [2][$\mathbf{BAr^F_4}$]−[4][$\mathbf{BAr^F_4}$] and Total Spin Populations $|\rho_{tot}|$ from Hyperfine Decomposition Analysis[a]

complex[b]		A_x	A_y	A_z	a_{iso}	$\lvert\rho_{tot}\rvert$
[**2**][$\mathbf{BAr^F_4}$]	$^{95/97}Mo$	95	75	155	107	
	$^{31}P_A$	35	72	20	42	
	$^{31}P_B$	46	35	20	34	
	$^{13}C_A$	24	30	20	25	
	$^{13}C_B$	40	20	35	32	
[**3**][$\mathbf{BAr^F_4}$]	$^{95/97}Mo$	86	86	165	110	0.64
	$^{31}P_A$	15	48	10	24	
	$^{31}P_B$	15	48	10	24	
	$^{13}C_A$	27.5	27.5	22.5	26	0.05−0.07[c]
	$^{13}C_B$	31	18	33	27	
[**4**][$\mathbf{BAr^F_4}$]	$^{95/97}Mo$	100	100	190	130	0.77
	$^{31}P_A$	60	70	60	63	
	$^{31}P_B$	60	70	60	63	
	^{13}C	31	31	17	26	0.08

[a]Signals observed for the ^{31}P and ^{13}C nuclei cannot be definitively assigned and thus are denoted A and B. [b]The hyperfine coupling tensors for [**2**][$\mathbf{BAr^F_4}$] were estimated through simulations of CW-EPR spectra; tensors for [**3**][$\mathbf{BAr^F_4}$] and [**4**][$\mathbf{BAr^F_4}$] were refined via simulation of the Davies ENDOR and HYSCORE spectra; see Figures S21−S32. [c]Estimated spin density for the carbyne C31.

https://doi.org/10.1021/jacs.1c03806
J. Am. Chem. Soc. 2021, 143, 13091−13102

Decomposition of the $^{95/97}$Mo hyperfine coupling tensors revealed a sequential increase in the spin density at Mo in the order [**1**][**BAr$^F_4$**] < [**3**][**BAr$^F_4$**] < [**4**][**BAr$^F_4$**], with a total of 0.58, 0.66, and 0.77 e$^-$ residing in Mo 4d_{xy} (Table 4). Spin delocalization onto the carbide and carbyne ligand, in contrast, remained nearly invariant across the series (0.05−0.09 e$^-$ on C_α). As in [**1**][**BAr$^F_4$**] and [**K**][**1**] above, the majority of the spin on C_α resides in 2p orbitals, with only ∼0.007 e$^-$ in C 2s for [**3**][**BAr$^F_4$**] and [**4**][**BAr$^F_4$**]. DFT calculations support a similar bonding picture to that described for [**1**][**BAr$^F_4$**] above. The calculated Löwdin spin populations agree with the values determined by EPR above (Table 5).

Table 5. Calculated Löwdin Spin Distributions (BP86/def2-TZVP) for Open-Shell Complexes Studied Herein[a]

	[**1**]$^+$	[**2**]$^+$	[**3**]$^+$	[**4**]$^+$	[**1**]$^-$
Mo1	0.55	0.69	0.64	0.72	0.02
C31 (carbide)	−0.07	−0.08	−0.07	−0.07	0.02
C32 (CO)	0.07	0.10	0.11		0.002
O1	0.05	0.06	0.08		−0.001
Cl1		0.15	0.15	0.09	
P1 = P2	0.04	0.03	0.03	0.01	0.02
C1−C6 (arene)	0.30	0	0	0.20	0.37

[a]For spin density plots, see Figure 7; spin densities calculated from EPR spin decomposition analysis are presented in Tables 2 and 4.

Besides [**2**][**BAr$^F_4$**]−[**4**][**BAr$^F_4$**], very few open-shell carbyne complexes have been studied by EPR, but the results presented herein suggest some commonalities. The C_{3v}-symmetric Fe^V carbyne [(SiP$_3$)Fe(≡CCH$_3$)][OTf] (where SiP$_3$ = tris(phosphino)silyl ligand) was found to exhibit an axial signal at 10 K with $g_\parallel$ at 2.61 and $g_\perp$ at 1.96−1.93.[47] The ^{13}C hyperfine coupling vector for the carbyne ($|A(^{13}C_\alpha)|$ = [18, 33, 47] MHz) indicated relatively minor amounts of spin delocalization onto that carbon, and indeed a spin decomposition analysis revealed relatively little spin density in C 2s (0.009 e$^-$) and more significant spin density in 2p$_x$ and 2p$_y$ (−0.07 e$^-$). The majority of the unpaired spin was instead located on Fe (0.99 e$^-$) in an orbital of $d_{x^2-y^2}$ parentage perpendicular to the Fe−C bond vector. Likewise, in the μ^2-C-bridged diiron carbyne complexes {Fe$_2$(μ^2-CAr)}[17] and {Fe$_2$(μ^2-CAr)}[19], only 0.009 e$^-$ was found in C 2s, with 0.03−0.04 e$^-$ in C 2p(π).[54] Finally, the tungsten methylidyne cation [(dmpe)$_2$(Cl)W(≡CH)]$^+$ was studied with g_{iso} = 2.026, $|a_{iso}(^{183}W)|$ = 221 MHz, $|a_{iso}(^{31}P)|$ = 149 MHz, and $|a_{iso}(^{13}C)|$ = 34 MHz.[48] While the anisotropic hyperfine coupling constants for this complex were not determined, the combined spectroscopic data indicated that the unpaired electron in [(dmpe)$_2$(Cl)W(≡CH)]$^+$ resides predominantly at W in an orbital of d_{xy} parentage perpendicular to the W≡C bond vector. The magnitude of $|a_{iso}(^{13}C)|$ also suggested a similar amount of spin delocalization to the carbyne C_α relative to other studied complexes.

C−C Coupling Reactivity. In preliminary reactivity studies, we observed that while the Mo(IV) carbide **1** is resistant to C−C coupling (and instead converts to isomeric **1′** on warming),[66] reduced [**K**][**1**] couples to form C−C bridged [**5**]$^{3-}$ (Figure 10). Thus, attempts to crystallize [**K**][**1**] in the absence of crown ethers over days at −40 °C resulted instead in crystallization of [**5**]$^{3-}$, together with dimeric units of ([**1**]$_2$)$^{3-}$ bridged in a polymeric unit with 1.5 K$^+$ per Mo (for the full structure, see Figure S52). While the more reduced

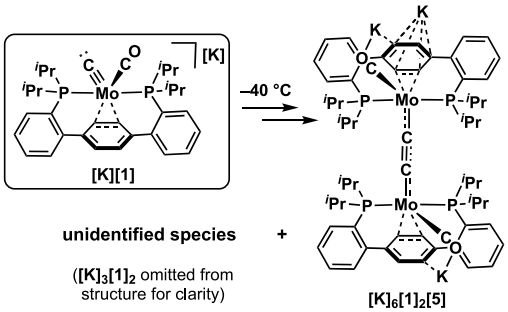

Figure 10. Intramolecular coupling of [**K**][**1**] to produce C−C bridged [**5**]$^{3-}$. Not shown is a dimeric unit of ([**1**]$_2$)$^{3-}$, cocrystallized as a coordination polymer with [**5**]$^{3-}$ and 6 K$^+$ per 4 Mo. Structure determination by single-crystal XRD; the crystal quality was insufficient to allow reliable determination of bond metrics.

charge state relative to the starting [**K**][**1**] indicates that disproportionation has occurred, the formation of coupled [**5**]$^{3-}$ showcases reactivity manifolds that are not accessible to the Mo(IV) carbides.

C−C coupling reactivity was likewise observed from less reduced charge states. Thus, following treatment of thawing solutions of carbide **1′** with $KC_{10}H_8$ (0.5 equiv) at −40 °C, C−C coupled [**K**][**6**] crystallized from the reaction mixture over a period of days (Figure 11). [**K**][**6**] was also observed starting from **1**, but this reaction necessitated longer reaction times (∼6 weeks at −40 °C), suggesting that initial conversion to **1′** was prerequisite to C−C coupling. Both [**K**]$_6$[**1**]$_2$[**5**] and [**K**][**6**] demonstrate the ability of reduced Mo carbides to

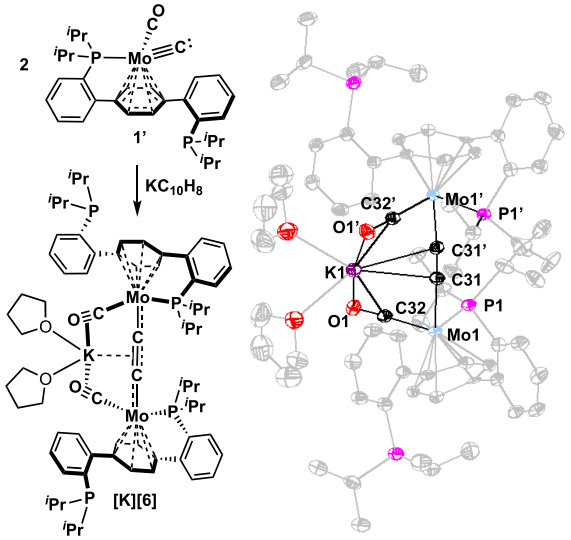

Figure 11. C−C coupling of **1′** on reduction with 0.5 equiv of $KC_{10}H_8$. Solid-state structure of coupled product [**K**][**6**] shown with thermal anisotropic displacement parameters at the 50% probability level; H atoms and free solvent molecules are omitted for clarity. Carbon atoms and bonds in bound THF molecules and P2 ligand shown in gray for clarity. Key bond lengths (Å) and angles (deg): Mo1−C31 2.091(5); C31−C31′ 1.254(7); Mo1−C32 1.955(5); C32−O1 1.169(6); Mo1−P1 2.430(1); C31−K1 3.019; C32−K1 3.036; O1−K1 2.987; Mo−C31−C31′ 176.9(4); Mo−C32−O1 177.3(4).

https://doi.org/10.1021/jacs.1c03806
J. Am. Chem. Soc. 2021, 143, 13091−13102

couple in mixed valence states, perhaps implicating a nucleophile/electrophile-type coupling pathway[80] in which the nucleophilicity of the terminal carbide ligand is enhanced through reduction by 1 e^-. This proposal is consistent with the low spin delocalization on the reduced carbides, which may be insufficient to promote coupling via a radical pathway. Regardless of the mechanism involved, these results illustrate the intimate relationship between redox state, spin delocalization, and reactivity in terminal, transition metal carbides, similarly to that observed in other open-shell complexes with metal−ligand multiple bonds.

Spin Delocalization in Open-Shell M≡C Complexes: Trends. The EPR and DFT results indicate a close correspondence in the electronic structures of the d^1 square-pyramidal carbides and carbynes studied. While the unpaired spin rests primarily in the SOMO of Mo d_{xy} parentage, non-negligible delocalization is also observed to the carbide/carbyne C_α (ca. 0.06−0.09 e^-).

For compounds [**2**][$\mathbf{BAr^F_4}$] and [**3**][$\mathbf{BAr^F_4}$], the SOMO displays π^* and π-backbonding character with respect to the Mo−Cl and Mo−CO interactions, respectively, resulting in spin delocalization onto these ligands (0.05−0.11 e^- on C32; 0.09−0.15 e^- on Cl1; Table 5). In [**1**][$\mathbf{BAr^F_4}$] and [**4**][$\mathbf{BAr^F_4}$], significant spin density is conferred on the central arene ring via the direct Mo−arene contact. In fact, this is the major spin location (0.20−0.22 e^-) aside from the metal. As shown in the crystal structure of [**4**][$\mathbf{BAr^F_4}$], loss of CO orients the carbyne cis to the arene and promotes π-backbonding with a double bond of the arene. Consequently, the SOMO has a substantial contribution from the arene. Because the SOMO is non-bonding with respect to the two phosphines, a smaller amount of spin density is transferred onto these atoms (0.01−0.04 e^-) in the [**1**][$\mathbf{BAr^F_4}$]-[**4**][$\mathbf{BAr^F_4}$] series.

The variation in spin density at Mo from ∼0.58−0.77 e^- in [**1**][$\mathbf{BAr^F_4}$]−[**4**][$\mathbf{BAr^F_4}$] is therefore not strongly correlated to the extent of spin delocalization to the carbide/carbyne C_α (0.05−0.09 e^-). Instead, the spin density at Mo is heavily influenced by the extent of delocalization onto the associated Cl, CO, and η^2-arene ligands. The substituents at C_α (lone pair, H, and $SiMe_3$) also do not have a strong impact. In contrast, the dimethylamide-substituted Fe carbyne [(SiP_3)-Fe(≡$CNMe_2$)][OTf], which has a close structural correspondence and identical d electron count with the methyl-substituted analogue [(SiP_3)Fe(≡CCH_3)][OTf], has only 0.03 e^- of spin localized at C_α (vs 0.07 e^- for the methyl-substituted analogue).[47,49] Reduced spin delocalization to C_α likely reflects the electron-donating capacity of the $-NMe_2$ group, which results in a significant [Fe]=C=NMe_2 resonance form.[49,50]

Carbide [**1**][$\mathbf{BAr^F_4}$] and silylcarbyne [**4**][$\mathbf{BAr^F_4}$] also share a close structural and electronic correspondence with the open-shell phosphide complex [P2Mo(≡P:)(Cl)][BAr^F_4], which has 0.65 e^- of unpaired spin in Mo $4d_{xy}$.[18] 0.10−0.14 e^- of spin density is delocalized to the terminal phosphide. Relative to the most structurally related complex [**4**][$\mathbf{BAr^F_4}$], the greater extent of spin delocalization onto the terminal phosphide most likely reflects the reduced electronegativity of P. A similar trend was observed in two structurally similar diiron complexes bearing μ^2-C and μ^2-N ligands.[54,81] Spin delocalization of −0.05 e^- was observed on the μ^2-C ligand vs −0.02 e^- on the more electronegative μ^2-N atom.[54,81]

An approach to increase spin localization on the multiply bonded terminal ligand is to increase the d-count at the metal to populate π antibonding orbitals. Such systems with terminal oxide and nitride ligands have been reported to localize up to 0.75 e^- on these ligands.[16,24−27] With terminal carbide ligands, only formally d^0, d^1, and d^2 systems have been reported. Compound [**K**][**1**] is formally Mo(III), d^3. However, EPR, DFT, and crystallography studies are consistent with primary localization of the spin on the terphenyl ligand, toward a formal Mo(IV), d^2 resonance structure. Notably, the reduction of the arene is preferred to populating Mo−C π antibonding orbitals and destabilizing that interaction, despite the relatively negative redox potential of the terphenyl arene (unsubstituted *p*-terphenyl: −2.45 V).[82] Moreover, the more electron-rich compound [**K**][**1**] has lower radical character on the carbide C than the oxidized analogue, [**1**][$\mathbf{BAr^F_4}$]. This is in line with measurements on metal−oxo,[83] nitride,[17] and bridged carbyne[54] species showing increased radical character at the higher metal oxidation state due to increased covalency, similarly to what is found in the present systems.

CONCLUSIONS

Herein, we report the preparation of five new radical carbide and carbyne complexes, including the first two known examples of open-shell, terminal carbides, [**1**][$\mathbf{BAr^F_4}$] and [**K**][**1**] (**1** = [P2Mo(≡C:)(CO)]). Access to this redox series of carbides and carbynes was enabled through the non-innocence of the P2 ligand. The P2 ligand is capable of providing stabilizing metal−arene interactions and absorbing excess reducing equivalents into the terphenyl arene unit. These compounds were characterized by in-depth pulse EPR experiments combined with DFT analysis and crystallography. These studies revealed predominantly metal-centered radicals in oxidized complexes [**1**][$\mathbf{BAr^F_4}$]−[**4**][$\mathbf{BAr^F_4}$], with 0.55−0.77 e^- on Mo depending on the extent of delocalization onto the accompanying Cl, CO, and η^2-arene ligands. Spin delocalization to the carbide ligand remains approximately constant at 0.05−0.09 e^- in all of these cases. Although small, this value is not insignificant. For example, an open-shell terminal phosphide supported on the same framework with 0.10−0.14 e^- on P undergoes P−P coupling chemistry even below room temperature.[18]

The combined EPR and DFT studies revealed a different picture for [**K**][**1**], however. The availability of low-lying empty orbitals in the arene system enables terphenyl reduction prior to population of the Mo≡C: π^* orbital, an indication of the strength of the Mo−C interaction. Notably, the more electron-deficient [**1**][$\mathbf{BAr^F_4}$] has a higher spin density on the carbide C than the two-electron-reduced [**K**][**1**], where the extra electrons fail to populate M−C antibonding orbitals. Moreover, [**K**][**1**] is significantly more stable than oxidized [**1**][$\mathbf{BAr^F_4}$], presumably because of storage of the unpaired electron in the terphenyl arene system and the lower spin density on the C. This behavior mirrors that of reactive metal−oxo and nitrido species with higher d-electron counts which undergo coupling and radical chemistry. These studies highlight a ligand-centered approach for potentially stabilizing reduced carbide analogues against undesired radical pathways.

Finally, the ability of the radical [**K**][**1**] to undergo C−C coupling is probed in preliminary reactivity studies. Presented are two C−C bridged dimers that reveal preferential formation of mixed-valent products. These examples illustrate the propensity for reduced carbides to undergo coupling chemistry and how productive reactivity profiles may be accessed through the manipulation of redox states.

https://doi.org/10.1021/jacs.1c03806
J. Am. Chem. Soc. 2021, 143, 13091−13102

■ ASSOCIATED CONTENT

Supporting Information

The Supporting Information is available free of charge at https://pubs.acs.org/doi/10.1021/jacs.1c03806.

Detailed experimental procedures, full characterization, and spectroscopic data (PDF)

Accession Codes

CCDC 2076055, 2076057−2076058, and 2076060 contain the supplementary crystallographic data for this paper. These data can be obtained free of charge via www.ccdc.cam.ac.uk/data_request/cif, or by emailing data_request@ccdc.cam.ac.uk, or by contacting The Cambridge Crystallographic Data Centre, 12 Union Road, Cambridge CB2 1EZ, UK; fax: +44 1223 336033.

■ AUTHOR INFORMATION

Corresponding Author

Theodor Agapie − *Division of Chemistry and Chemical Engineering, California Institute of Technology, Pasadena, California 91125, United States;* orcid.org/0000-0002-9692-7614; Email: agapie@caltech.edu

Authors

Gwendolyn A. Bailey − *Division of Chemistry and Chemical Engineering, California Institute of Technology, Pasadena, California 91125, United States*

Joshua A. Buss − *Division of Chemistry and Chemical Engineering, California Institute of Technology, Pasadena, California 91125, United States;* orcid.org/0000-0002-3347-8583

Paul H. Oyala − *Division of Chemistry and Chemical Engineering, California Institute of Technology, Pasadena, California 91125, United States;* orcid.org/0000-0002-8761-4667

Complete contact information is available at: https://pubs.acs.org/10.1021/jacs.1c03806

Notes

The authors declare no competing financial interest.

■ ACKNOWLEDGMENTS

We thank Lawrence Henling, Michael Takase, and Manar Shoshani for invaluable crystallographic assistance. Lawrence Henling is also thanked for assistance with elemental analysis. G.A.B. is grateful to NSERC of Canada and the Resnick Sustainability Institute at Caltech for fellowship support. J.A.B. is grateful for an NSF graduate research fellowship. We thank the NSF (CHE-1800501), the Dow Next Generation Education Fund (instrumentation), and Caltech for funding.

■ REFERENCES

(1) Ortiz de Montellano, P. R., Ed.; *Cytochrome P450: Structure, Mechanism, and Biochemistry*, 4th ed.; Kluwer Academic/Plenum Publishers: New York, 2005; pp 1−43.

(2) Krebs, C.; Galonić Fujimori, D.; Walsh, C. T.; Bollinger, J. M. Non-Heme Fe(IV)−Oxo Intermediates. *Acc. Chem. Res.* **2007**, *40* (7), 484−492.

(3) Chatt, J.; Dilworth, J. R.; Richards, R. L. Recent advances in the chemistry of nitrogen fixation. *Chem. Rev.* **1978**, *78* (6), 589−625.

(4) Chalkley, M. J.; Drover, M. W.; Peters, J. C. Catalytic N_2-to-NH_3 (or -N_2H_4) Conversion by Well-Defined Molecular Coordination Complexes. *Chem. Rev.* **2020**, *120* (12), 5582−5636.

(5) Spasyuk, D. M.; Carpenter, S. H.; Kefalidis, C. E.; Piers, W. E.; Neidig, M. L.; Maron, L. Facile hydrogen atom transfer to iron(III) imido radical complexes supported by a dianionic pentadentate ligand. *Chem. Sci.* **2016**, *7* (9), 5939−5944.

(6) Cowley, R. E.; DeYonker, N. J.; Eckert, N. A.; Cundari, T. R.; DeBeer, S.; Bill, E.; Ottenwaelder, X.; Flaschenriem, C.; Holland, P. L. Three-Coordinate Terminal Imidoiron(III) Complexes: Structure, Spectroscopy, and Mechanism of Formation. *Inorg. Chem.* **2010**, *49* (13), 6172−6187.

(7) Cowley, R. E.; Holland, P. L. Ligand Effects on Hydrogen Atom Transfer from Hydrocarbons to Three-Coordinate Iron Imides. *Inorg. Chem.* **2012**, *51* (15), 8352−8361.

(8) Bart, S. C.; Lobkovsky, E.; Bill, E.; Chirik, P. J. Synthesis and Hydrogenation of Bis(imino)pyridine Iron Imides. *J. Am. Chem. Soc.* **2006**, *128* (16), 5302−5303.

(9) Scepaniak, J. J.; Young, J. A.; Bontchev, R. P.; Smith, J. M. Formation of Ammonia from an Iron Nitrido Complex. *Angew. Chem., Int. Ed.* **2009**, *48* (17), 3158−3160.

(10) Lu, C. C.; Saouma, C. T.; Day, M. W.; Peters, J. C. Fe(I)-Mediated Reductive Cleavage and Coupling of CO_2: An $Fe^{II}(\mu$-O,μ-CO)Fe^{II} Core. *J. Am. Chem. Soc.* **2007**, *129* (1), 4−5.

(11) Betley, T. A.; Peters, J. C. Dinitrogen Chemistry from Trigonally Coordinated Iron and Cobalt Platforms. *J. Am. Chem. Soc.* **2003**, *125* (36), 10782−10783.

(12) Carsch, K. M.; DiMucci, I. M.; Iovan, D. A.; Li, A.; Zheng, S.-L.; Titus, C. J.; Lee, S. J.; Irwin, K. D.; Nordlund, D.; Lancaster, K. M.; Betley, T. A. Synthesis of a copper-supported triplet nitrene complex pertinent to copper-catalyzed amination. *Science* **2019**, *365* (6458), 1138.

(13) Dong, Y.; Clarke, R. M.; Zheng, S.-L.; Betley, T. A. Synthesis and electronic structure studies of a Cr-imido redox series. *Chem. Commun.* **2020**, *56* (21), 3163−3166.

(14) Dong, Y.; Lund, C. J.; Porter, G. J.; Clarke, R. M.; Zheng, S.-L.; Cundari, T. R.; Betley, T. A. Enantioselective C−H Amination Catalyzed by Nickel Iminyl Complexes Supported by Anionic Bisoxazoline (BOX) Ligands. *J. Am. Chem. Soc.* **2021**, *143* (2), 817−829.

(15) Chang, H.-C.; Lin, Y.-H.; Werlé, C.; Neese, F.; Lee, W.-Z.; Bill, E.; Ye, S. Conversion of a Fleeting Open-Shell Iron Nitride into an Iron Nitrosyl. *Angew. Chem., Int. Ed.* **2019**, *58* (49), 17589−17593.

(16) Chang, H.-C.; Mondal, B.; Fang, H.; Neese, F.; Bill, E.; Ye, S. Electron Paramagnetic Resonance Signature of Tetragonal Low Spin Iron(V)-Nitrido and -Oxo Complexes Derived from the Electronic Structure Analysis of Heme and Non-Heme Archetypes. *J. Am. Chem. Soc.* **2019**, *141* (6), 2421−2434.

(17) Clarke, R. M.; Storr, T. Tuning Electronic Structure To Control Manganese Nitride Activation. *J. Am. Chem. Soc.* **2016**, *138* (47), 15299−15302.

(18) Buss, J. A.; Oyala, P. H.; Agapie, T. Terminal Molybdenum Phosphides with d Electrons: Radical Character Promotes Coupling Chemistry. *Angew. Chem., Int. Ed.* **2017**, *56* (46), 14502−14506.

(19) Brown, S. D.; Mehn, M. P.; Peters, J. C. Heterolytic H_2 Activation Mediated by Low-Coordinate L_3Fe-(μ-N)-FeL_3 Complexes to Generate Fe(μ-NH)(μ-H)Fe Species. *J. Am. Chem. Soc.* **2005**, *127* (38), 13146−13147.

(20) Astashkin, A. V.; Neese, F.; Raitsimring, A. M.; Cooney, J. J. A.; Bultman, E.; Enemark, J. H. Pulsed EPR Investigations of Systems Modeling Molybdenum Enzymes: Hyperfine and Quadrupole Parameters of Oxo-^{17}O in [$Mo^{17}O(SPh)_4$]. *J. Am. Chem. Soc.* **2005**, *127* (47), 16713−16722.

(21) Cutsail, G. E., III; Stein, B. W.; Subedi, D.; Smith, J. M.; Kirk, M. L.; Hoffman, B. M. EPR, ENDOR, and Electronic Structure Studies of the Jahn−Teller Distortion in an Fe^V Nitride. *J. Am. Chem. Soc.* **2014**, *136* (35), 12323−12336.

(22) Similarly, only 0.07 e^- were found on a terminal nitrido in the d1 trigonal-bipyramidal complex [Mo(N)(trisamidoamine)]$^-$, with the balance of spin density found on the metal in an orbital of Mo d_{xy} parentage. See: Sharma, A.; Roemelt, M.; Reithofer, M.; Schrock, R. R.; Hoffman, B. M.; Neese, F. EPR/ENDOR and Theoretical Study

of the Jahn−Teller-Active [HIPTN$_3$N]MoVL Complexes (L = N−, NH). *Inorg. Chem.* **2017**, *56* (12), 6906−6919.
(23) Scepaniak, J. J.; Vogel, C. S.; Khusniyarov, M. M.; Heinemann, F. W.; Meyer, K.; Smith, J. M. Synthesis, Structure, and Reactivity of an Iron(V) Nitride. *Science* **2011**, *331* (6020), 1049.
(24) Berry, J. F.; Bill, E.; Bothe, E.; George, S. D.; Mienert, B.; Neese, F.; Wieghardt, K. An Octahedral Coordination Complex of Iron(VI). *Science* **2006**, *312* (5782), 1937−1941.
(25) Aliaga-Alcalde, N.; DeBeer George, S.; Mienert, B.; Bill, E.; Wieghardt, K.; Neese, F. The Geometric and Electronic Structure of [(cyclam-acetato)Fe(N)]$^+$: A Genuine Iron(V) Species with a Ground-State Spin S = 1/2. *Angew. Chem., Int. Ed.* **2005**, *44* (19), 2908−2912.
(26) Scheibel, M. G.; Askevold, B.; Heinemann, F. W.; Reijerse, E. J.; de Bruin, B.; Schneider, S. Closed-shell and open-shell square-planar iridium nitrido complexes. *Nat. Chem.* **2012**, *4* (7), 552−558.
(27) Zolnhofer, E. M.; Käß, M.; Khusniyarov, M. M.; Heinemann, F. W.; Maron, L.; van Gastel, M.; Bill, E.; Meyer, K. An Intermediate Cobalt(IV) Nitrido Complex and its N-Migratory Insertion Product. *J. Am. Chem. Soc.* **2014**, *136* (42), 15072−15078.
(28) Krusic, P. J.; Klabunde, U.; Casey, C. P.; Block, T. F. An electron spin resonance study of the radical anions derived from metal carbene complexes of chromium, molybdenum, and tungsten. *J. Am. Chem. Soc.* **1976**, *98* (7), 2015−2018.
(29) Dzik, W. I.; Xu, X.; Zhang, X. P.; Reek, J. N. H.; de Bruin, B. 'Carbene Radicals' in Co^{II}(por)-Catalyzed Olefin Cyclopropanation. *J. Am. Chem. Soc.* **2010**, *132* (31), 10891−10902.
(30) Cui, X.; Xu, X.; Jin, L.-M.; Wojtas, L.; Zhang, X. P. Stereoselective radical C−H alkylation with acceptor/acceptor-substituted diazo reagents via Co(II)-based metalloradical catalysis. *Chem. Sci.* **2015**, *6* (2), 1219−1224.
(31) King, E. R.; Hennessy, E. T.; Betley, T. A. Catalytic C−H Bond Amination from High-Spin Iron Imido Complexes. *J. Am. Chem. Soc.* **2011**, *133* (13), 4917−4923.
(32) Baek, Y.; Betley, T. A. Catalytic C−H Amination Mediated by Dipyrrin Cobalt Imidos. *J. Am. Chem. Soc.* **2019**, *141* (19), 7797−7806.
(33) Baek, Y.; Hennessy, E. T.; Betley, T. A. Direct Manipulation of Metal Imido Geometry: Key Principles to Enhance C−H Amination Efficacy. *J. Am. Chem. Soc.* **2019**, *141* (42), 16944−16953.
(34) Dzik, W. I.; Zhang, X. P.; de Bruin, B. Redox Noninnocence of Carbene Ligands: Carbene Radicals in (Catalytic) C−C Bond Formation. *Inorg. Chem.* **2011**, *50* (20), 9896−9903.
(35) Das, B. G.; Chirila, A.; Tromp, M.; Reek, J. N. H.; de Bruin, B. Co^{III}−Carbene Radical Approach to Substituted ^{1}H-Indenes. *J. Am. Chem. Soc.* **2016**, *138* (28), 8968−8975.
(36) Chirila, A.; Gopal Das, B.; Paul, N. D.; de Bruin, B. Diastereoselective Radical-Type Cyclopropanation of Electron-Deficient Alkenes Mediated by the Highly Active Cobalt(II) Tetramethyltetraaza[14]annulene Catalyst. *ChemCatChem* **2017**, *9* (8), 1413−1421.
(37) te Grotenhuis, C.; van den Heuvel, N.; van der Vlugt, J. I.; de Bruin, B. Catalytic Dibenzocyclooctene Synthesis via Cobalt(III)−Carbene Radical and ortho-Quinodimethane Intermediates. *Angew. Chem., Int. Ed.* **2018**, *57* (1), 140−145.
(38) Hu, Y.; Lang, K.; Tao, J.; Marshall, M. K.; Cheng, Q.; Cui, X.; Wojtas, L.; Zhang, X. P. Next-Generation D_2-Symmetric Chiral Porphyrins for Cobalt(II)-Based Metalloradical Catalysis: Catalyst Engineering by Distal Bridging. *Angew. Chem., Int. Ed.* **2019**, *58* (9), 2670−2674.
(39) Zhou, M.; Lankelma, M.; van der Vlugt, J. I.; de Bruin, B. Catalytic Synthesis of 8-Membered Ring Compounds via Cobalt(III)-Carbene Radicals. *Angew. Chem., Int. Ed.* **2020**, *59* (27), 11073−11079.
(40) Chirila, A.; van Vliet, K. M.; Paul, N. D.; de Bruin, B. [Co(MeTAA)] Metalloradical Catalytic Route to Ketenes via Carbonylation of Carbene Radicals. *Eur. Eur. J. Inorg. Chem.* **2018**, *2018* (20−21), 2251−2258.
(41) Berry, J. F. Terminal nitrido and imido complexes of the late transition ketals. *Comments Inorg. Chem.* **2009**, *30* (1−2), 28−66.
(42) Gunay, A.; Theopold, K. H. C−H Bond Activations by Metal Oxo Compounds. *Chem. Rev.* **2010**, *110* (2), 1060−1081.
(43) Felixberger, J. K.; Kiprof, P.; Herdtweck, E.; Herrmann, W. A.; Jakobi, R.; Gütlich, P. Alkyl and Alkylidyne Complexes of Rhenium. *Angew. Chem., Int. Ed. Engl.* **1989**, *28* (3), 334−337.
(44) N. D. A. Lemos, M. A.; Pombeiro, A. J. L.; Hughes, D. L.; Richards, R. L. Synthesis and X-ray crystal structure of *trans*-[MoF(CCH$_2$^{t}Bu)(Ph$_2$PCH$_2$CH$_2$PPh$_2$)$_2$][BF$_4$], a paramagnetic alkylidynefluorocomplex. *J. Organomet. Chem.* **1992**, *434* (1), C6−C9.
(45) Manna, J.; Gilbert, T. M.; Dallinger, R. F.; Geib, S. J.; Hopkins, M. D. Nature of the frontier orbitals of tungsten benzylidyne complexes. *J. Am. Chem. Soc.* **1992**, *114* (14), 5870−5872.
(46) Colebatch, A. L.; Cordiner, R. L.; Hill, A. F.; Nguyen, K. T. H. D.; Shang, R.; Willis, A. C. A Bis-Carbyne (Ethanediylidyne) Complex via the Catalytic Demercuration of a Mercury Bis(carbido) Complex. *Organometallics* **2009**, *28* (15), 4394−4399.
(47) Citek, C.; Oyala, P. H.; Peters, J. C. Mononuclear Fe(I) and Fe(II) Acetylene Adducts and Their Reductive Protonation to Terminal Fe(IV) and Fe(V) Carbynes. *J. Am. Chem. Soc.* **2019**, *141* (38), 15211−15221.
(48) van der Eide, E. F.; Piers, W. E.; Parvez, M.; McDonald, R. Synthesis and Characterization of Cationic Tungsten(V) Methylidynes. *Inorg. Chem.* **2007**, *46* (1), 14−21.
(49) Rittle, J.; Peters, J. C. Proton-Coupled Reduction of an Iron Cyanide Complex to Methane and Ammonia. *Angew. Chem., Int. Ed.* **2016**, *55* (40), 12262−12265.
(50) Rittle, J.; Peters, J. C. N−H Bond Dissociation Enthalpies and Facile H Atom Transfers for Early Intermediates of Fe−N$_2$ and Fe−CN Reductions. *J. Am. Chem. Soc.* **2017**, *139* (8), 3161−3170.
(51) Arnett, C. H.; Agapie, T. Activation of an Open Shell, Carbyne-Bridged Diiron Complex Toward Binding of Dinitrogen. *J. Am. Chem. Soc.* **2020**, *142* (22), 10059−10068.
(52) Kim, H. P.; Angelici, R. J. Transition Metal Complexes with Terminal Carbyne Ligands. In *Advances in Organometallic Chemistry*; O'Malley, B. W., Ed.; Academic Press: 1987; Vol. *27*, pp 51−111.
(53) Fürstner, A.; Davies, P. W. Alkyne metathesis. *Chem. Commun.* **2005**, *18*, 2307−2320.
(54) Arnett, C. H.; Bogacz, I.; Chatterjee, R.; Yano, J.; Oyala, P. H.; Agapie, T. Mixed-Valent Diiron μ-Carbyne, μ-Hydride Complexes: Implications for Nitrogenase. *J. Am. Chem. Soc.* **2020**, *142* (44), 18795−18813.
(55) Caselli, A.; Solari, E.; Scopelliti, R.; Floriani, C. The Stepwise Four- and Six-Electron Reduction of Carbon Monoxide to Oxy-alkylidyne, to Carbide and Oxide, Then to Carbide over an Nb−Oxo Surface Modeled by Calix[4]arene1. *J. Am. Chem. Soc.* **2000**, *122* (3), 538−539.
(56) Hejl, A.; Trnka, T. M.; Day, M. W.; Grubbs, R. H. Terminal ruthenium carbido complexes as σ-donor ligands. *Chem. Commun.* **2002**, *21*, 2524−2525.
(57) Carlson, R. G.; Gile, M. A.; Heppert, J. A.; Mason, M. H.; Powell, D. R.; Velde, D. V.; Vilain, J. M. The Metathesis-Facilitated Synthesis of Terminal Ruthenium Carbide Complexes: A Unique Carbon Atom Transfer Reaction. *J. Am. Chem. Soc.* **2002**, *124* (8), 1580−1581.
(58) Stewart, M. H.; Johnson, M. J. A.; Kampf, J. W. Terminal Carbido Complexes of Osmium: Synthesis, Structure, and Reactivity Comparison to the Ruthenium Analogues. *Organometallics* **2007**, *26* (20), 5102−5110.
(59) Caskey, S. R.; Stewart, M. H.; Kivela, J. E.; Sootsman, J. R.; Johnson, M. J. A.; Kampf, J. W. Two Generalizable Routes to Terminal Carbido Complexes. *J. Am. Chem. Soc.* **2005**, *127* (48), 16750−16751.
(60) Peters, J. C.; Odom, A. L.; Cummins, C. C. A terminal molybdenum carbide prepared by methylidyne deprotonation. *Chem. Commun.* **1997**, *20*, 1995−1996.

https://doi.org/10.1021/jacs.1c03806
J. Am. Chem. Soc. 2021, 143, 13091−13102

(61) Enriquez, A. E.; White, P. S.; Templeton, J. L. Reactions of an Amphoteric Terminal Tungsten Methylidyne Complex. *J. Am. Chem. Soc.* **2001**, *123* (21), 4992−5002.
(62) Agapie, T.; Diaconescu, P. L.; Cummins, C. C. Methine (CH) Transfer via a Chlorine Atom Abstraction/Benzene-Elimination Strategy: Molybdenum Methylidyne Synthesis and Elaboration to a Phosphaisocyanide Complex. *J. Am. Chem. Soc.* **2002**, *124* (11), 2412−2413.
(63) Greco, J. B.; Peters, J. C.; Baker, T. A.; Davis, W. M.; Cummins, C. C.; Wu, G. Atomic Carbon as a Terminal Ligand: Studies of a Carbidomolybdenum Anion Featuring Solid-State ^{13}C NMR Data and Proton-Transfer Self-Exchange Kinetics. *J. Am. Chem. Soc.* **2001**, *123* (21), 5003−5013.
(64) Buss, J. A.; Agapie, T. Four-electron deoxygenative reductive coupling of carbon monoxide at a single metal site. *Nature* **2016**, *529* (7584), 72−75.
(65) Buss, J. A.; Agapie, T. Mechanism of Molybdenum-Mediated Carbon Monoxide Deoxygenation and Coupling: Mono- and Dicarbyne Complexes Precede C−O Bond Cleavage and C−C Bond Formation. *J. Am. Chem. Soc.* **2016**, *138* (50), 16466−16477.
(66) Buss, J. A.; Bailey, G. A.; Oppenheim, J.; VanderVelde, D. G.; Goddard, W. A.; Agapie, T. CO Coupling Chemistry of a Terminal Mo Carbide: Sequential Addition of Proton, Hydride, and CO Releases Ethenone. *J. Am. Chem. Soc.* **2019**, *141* (39), 15664−15674.
(67) Bao, J.; Yang, G.; Yoneyama, Y.; Tsubaki, N. Significant Advances in C_1 Catalysis: Highly Efficient Catalysts and Catalytic Reactions. *ACS Catal.* **2019**, *9*, 3026−3053.
(68) Miller, R. L.; Wolczanski, P. T.; Rheingold, A. L. Carbide formation via carbon monoxide dissociation across a tungsten-tungsten triple bond. *J. Am. Chem. Soc.* **1993**, *115* (22), 10422−10423.
(69) Tachikawa, M.; Muetterties, E. L. Metal clusters. 25. A uniquely bonded C-H group and reactivity of a low-coordinate carbidic carbon atom. *J. Am. Chem. Soc.* **1980**, *102* (13), 4541−4542.
(70) Takemoto, S.; Morita, H.; Karitani, K.; Fujiwara, H.; Matsuzaka, H. A Bimetallic Ru_2Pt Complex Containing a Trigonal-Planar μ^3-Carbido Ligand: Formation, Structure, and Reactivity Relevant to the Fischer−Tropsch Process. *J. Am. Chem. Soc.* **2009**, *131* (50), 18026−18027.
(71) Takemoto, S.; Ohata, J.; Umetani, K.; Yamaguchi, M.; Matsuzaka, H. A Diruthenium μ-Carbido Complex That Shows Singlet-Carbene-like Reactivity. *J. Am. Chem. Soc.* **2014**, *136* (45), 15889−15892.
(72) Surface carbynes and carbides have been posited as important intermediates in the industrially important Fischer−Tropsch synthesis, for which the mechanism is not fully understood. See: (a) Maitlis, P. M.; Zanotti, V. The role of electrophilic species in the Fischer−Tropsch reaction. *Chem. Commun.* **2009**, *45* (13), 1619−1634. (b) de Smit, E.; Weckhuysen, B. M. The renaissance of iron-based Fischer−Tropsch synthesis: on the multifaceted catalyst deactivation behaviour. *Chem. Soc. Rev.* **2008**, *37* (12), 2758−2781.
(73) Buss, J. A.; Cheng, C.; Agapie, T. A Low-Valent Molybdenum Nitride Complex: Reduction Promotes Carbonylation Chemistry. *Angew. Chem., Int. Ed.* **2018**, *57* (31), 9670−9674.
(74) McNaughton, R. L.; Roemelt, M.; Chin, J. M.; Schrock, R. R.; Neese, F.; Hoffman, B. M. Experimental and Theoretical EPR Study of Jahn−Teller-Active [HIPTN$_3$N]MoL Complexes (L = N_2, CO, NH_3). *J. Am. Chem. Soc.* **2010**, *132* (25), 8645−8656.
(75) Manikandan, P.; Choi, E.-Y.; Hille, R.; Hoffman, B. M. 35 GHz ENDOR Characterization of the "Very Rapid" Signal of Xanthine Oxidase Reacted with 2-Hydroxy-6-methylpurine ($^{13}C_8$): Evidence against Direct Mo−C_8 Interaction. *J. Am. Chem. Soc.* **2001**, *123* (11), 2658−2663.
(76) Morton, J. R.; Preston, K. F. Atomic parameters for paramagnetic resonance data. *J. Magn. Reson.* **1978**, *30* (3), 577−582.
(77) The extreme thermal sensitivity [**1**][**BAr$^F_4$**] (generated *in situ* in the EPR tube over 30 s at −130 °C) precludes generation of the mixed-isotope complexes by reaction with ^{13}CO and hence definitive assignment of the hyperfine tensors for these two nuclei.
(78) A similar configuration is observed in the kinetic silylcarbyne isomer of **3**, which forms at reduced temperatures on treatment of reduced dicarbonyl complex P2Mo(CO)$_2$K$_2$ with trimethylsilyl triflate. See ref 64.
(79) Owing to its structural and electronic similarity with [**3**][**BAr$^F_4$**] according to the combined EPR, DFT, and XRD data, [**2**][**BAr$^F_4$**] was not studied in detail by pulse EPR experiments.
(80) Seymore, S. B.; Brown, S. N. Polar Effects in Nitride Coupling Reactions. *Inorg. Chem.* **2002**, *41* (3), 462−469.
(81) Kinney, R. A.; Saouma, C. T.; Peters, J. C.; Hoffman, B. M. Modeling the Signatures of Hydrides in Metalloenzymes: ENDOR Analysis of a Di-iron Fe(μ-NH)(μ-H)Fe Core. *J. Am. Chem. Soc.* **2012**, *134* (30), 12637−12647.
(82) Das, S.; Balaraju, T.; Barman, S.; Sreejith, S. S.; Pochamoni, R.; Roy, S. A Molecular CO_2 Reduction Catalyst Based on Giant Polyoxometalate {Mo_{368}}. *Front. Chem.* **2018**, DOI: 10.3389/fchem.2018.00514.
(83) Gupta, R.; Taguchi, T.; Lassalle-Kaiser, B.; Bominaar, E. L.; Yano, J.; Hendrich, M. P.; Borovik, A. S. High-spin Mn−oxo complexes and their relevance to the oxygen-evolving complex within photosystem II. *Proc. Natl. Acad. Sci. U. S. A.* **2015**, *112* (17), 5319.

https://doi.org/10.1021/jacs.1c03806
J. Am. Chem. Soc. 2021, 143, 13091−13102